




Reconfiguration and oscillations of a vertical, cantilevered sheet subject to vortex shedding behind a cylinder

J. John Soundar Jerome ^{1,*}, Yann Bachelier,¹ Delphine Doppler,¹
Christoph Lehmann ¹ and Nicolas Rivière ²

¹Univ. Lyon, Université Claude Bernard Lyon 1, Laboratoire de Mécanique des Fluides et d'Acoustique, CNRS UMR-5509, Boulevard 11 novembre 1918, F-69622 Villeurbanne Cedex, Lyon, France

²INSA de Lyon, Laboratoire de Mécanique des Fluides et d'Acoustique, CNRS UMR-5509, Boulevard 11 novembre 1918, F-69622 Villeurbanne Cedex, Lyon, France



(Received 8 October 2022; accepted 14 July 2023; published 15 September 2023)

The dynamics of a thin low-density polyethylene sheet subject to periodic forcing due to Bénard-Kármán vortices in a long narrow water channel is investigated here. In particular, the time-averaged sheet deflection and its oscillation amplitude are considered. The former is first illustrated to be well-approximated by the static equilibrium between the buoyancy force, the elastic restoring force, and the profile drag based on the depth-averaged water speed. Our observations also indicate that the presence of upstream vortices hinder the overall reconfiguration effect, well-known in an otherwise steady flow. For the sheet-tip oscillations, a simple model based on a torsional-spring-mounted flat plate correctly captures the measured tip amplitude δ_b over a wide range of sheet physical properties and flow conditions. Furthermore, a rich phenomenology of structural dynamics including vortex-forced-vibration, lock-in with the sheet natural frequency, and flow-induced vibration due to the sheet wake, multiple-frequency, and modal response is reported.

DOI: [10.1103/PhysRevFluids.8.093801](https://doi.org/10.1103/PhysRevFluids.8.093801)

I. INTRODUCTION

A rigid circular cylinder, when exposed to a fluid flow, expresses a wide variety of dynamics depending on its mechanical properties, the flow characteristics, and its boundary conditions. Many investigations on the cylinder wake characteristics [1–4] and the related vortex induced vibration (VIV) [5–10] continue to contribute to a multitude of industrial applications, involving structural design in both marine and civil engineering, energy harvesting, locomotion, mixing, and transfer [11–14, among others]. Often in applications and in nature, mechanical structures that are exposed to a fluid flow could be very flexible in alleviating flow-generated forces [15–21]. The resulting internal bending stresses and the modified flow angle of attack might alter both the structural dynamics and the wake characteristics. Such effects have only recently been considered for flow-bent cylinders to explore associated fluid structure interactions, namely, reduction in oscillation amplitude, multifrequency response, and *lock-in* mode, to name a few [22, and references therein]. While, a related topic, namely, the flutter of a flat plate, be it rigid or flexible, has received a lot of attention during the past two decades [23, for more], rare are the studies on VIV of a single cantilevered slender blades whose one end is anchored to the flow bed.

In this context, using single specimens of four different freshwater plants in laboratory flumes whose floor is covered with uniform density of shorter artificial grass, Siniscalchi and Nikora [24] correlated individual plant movement and its drag-force fluctuations with respect to upstream

*john-soundar@univ-lyon1.fr; <https://lmfa.ec-lyon.fr/spip.php?article378>

turbulence. Also, they reported spatial flappinglike movement in all plant species, with the propagation velocity of perturbations being comparable to the approach flow velocity. More recently, a series of studies by Jin *et al.* [25–28] put light upon a rich phenomenology of fluid-structure interactions for dynamically *reconfigured* flexible blades. Jin *et al.* [25] pointed out that moderately long flexible structures [aspect ratio $L_b/w_b \in (5, 25)$] vibrate in the streamwise direction at their natural frequency while the wake fluctuations beat at frequency of vortex shedding. Jin *et al.* [26] also illustrated that the structural dynamics of moderately short flexible plates [aspect ratio $L_b/w_b \in (2, 3)$] are governed by both wake fluctuations and nonlinear modulations of structural bending. These cantilevered structures presented a maximum tip oscillation intensity at some critical Cauchy number which compares the profile drag force experienced by the structure if it were rigid and the characteristic internal restoring force generated due to an external force. More recently, Jin *et al.* [28] used a flexible blade of aspect ratio $L_b/w_b = 4$ at different inclination angles to the incoming flow and highlighted the presence of three modes of tip oscillations, namely, fluttering, tip twisting, and orbital modes which occur, respectively, at increasing Cauchy number C_y . Orbital modes are characterized by large-amplitude coupled twisting and bending deformations, and they occur for sufficiently large inclination angles. Much is to follow in the perspective of these studies, for instance, the influence of mass ratio, Reynolds and Cauchy numbers on the sheet reconfiguration, and sheet tip dynamics such as oscillation amplitudes and frequency content.

The effect of wind on trees and terrestrial plant fields and of water currents on aquatic vegetation [20,21,29] are crucial for sediment transport, water quality, and biodiversity of aquatic species. Among the well-known examples, *honami* (Japanese: *ho* = crops and *nami* = wave) [30–32] and *monami* (Japanese: *mo* = aquatic plant) [33–36], respectively, represent coherent motion of crops and aquatic canopies when the flow resistance is sufficiently high. The proposed mechanistic views of such wavy motion generally involve the two-way coupling between flow vortices and the flexible canopy of plants [20,29,37], so the velocity spectrum and eddies in the incoming flow modulate the motion of flexible structures [38]. Also, there is now some evidence [39, Chap. 5] that the mechanical response of flexible blades in a channel flow might depend strongly on the Cauchy number C_y . It seems, therefore, important to know how vortices of different sizes interact with cantilevered flexible blades at various flow velocities and blade physical characteristics.

In the wake of these previous investigations, we propose to study the motion of a thin flexible sheet anchored to the bottom of a water channel when it encounters a regular array of eddies generated from vortex shedding behind a cylinder (Fig. 1). Thereby, we seek to provide a few insights into the *dynamic* reconfiguration (Sec. III), tip amplitude (Sec. IV), and tip frequency (Sec. V) for a good range of Cauchy numbers. While our experiments were first built in the hope of modeling the behavior of plant canopies that interact with flow vortices to exhibit coherent motion such as *honami* and *monami*, we believe that our set-up and findings also pave way to explore a whole other kind of fluid-structure interaction phenomena that could be referred to as *vortex forced vibration*.

II. MATERIALS, SETUP, AND METHODS

All experiments are performed in a long-narrow water channel as schematized in Fig. 1(a). Water from the pump (700 – 2800 lit/h) passes through a fine grid in the inlet and flows out into a narrow two-meter long channel of width 4 cm and height 25 cm. By properly adjusting the outlet gate and the horizontal slope of the channel, it is possible to maintain a free-surface flow of uniform water height across the entire channel. At a little more than one meter, a circular cylinder of diameter d_0 is fixed with its axis parallel to the floor but perpendicular to the flow. Behind the cylinder (downstream), a thin flexible rectangular sheet is fixed firmly to the channel bottom. The sheet’s foot is fixed at a distance $3d_0$ from the cylinder’s center, so a well-developed vortex street is set up [1,40] in front of the sheet while the latter does not influence the cylinder’s wake flow. Finally, to avoid the effect of free surface on the vortex-forced oscillations of the sheet and, also, for the sake of simplicity, the cylinder’s vertical location is taken as h_0 equal to the sheet height in a steady,

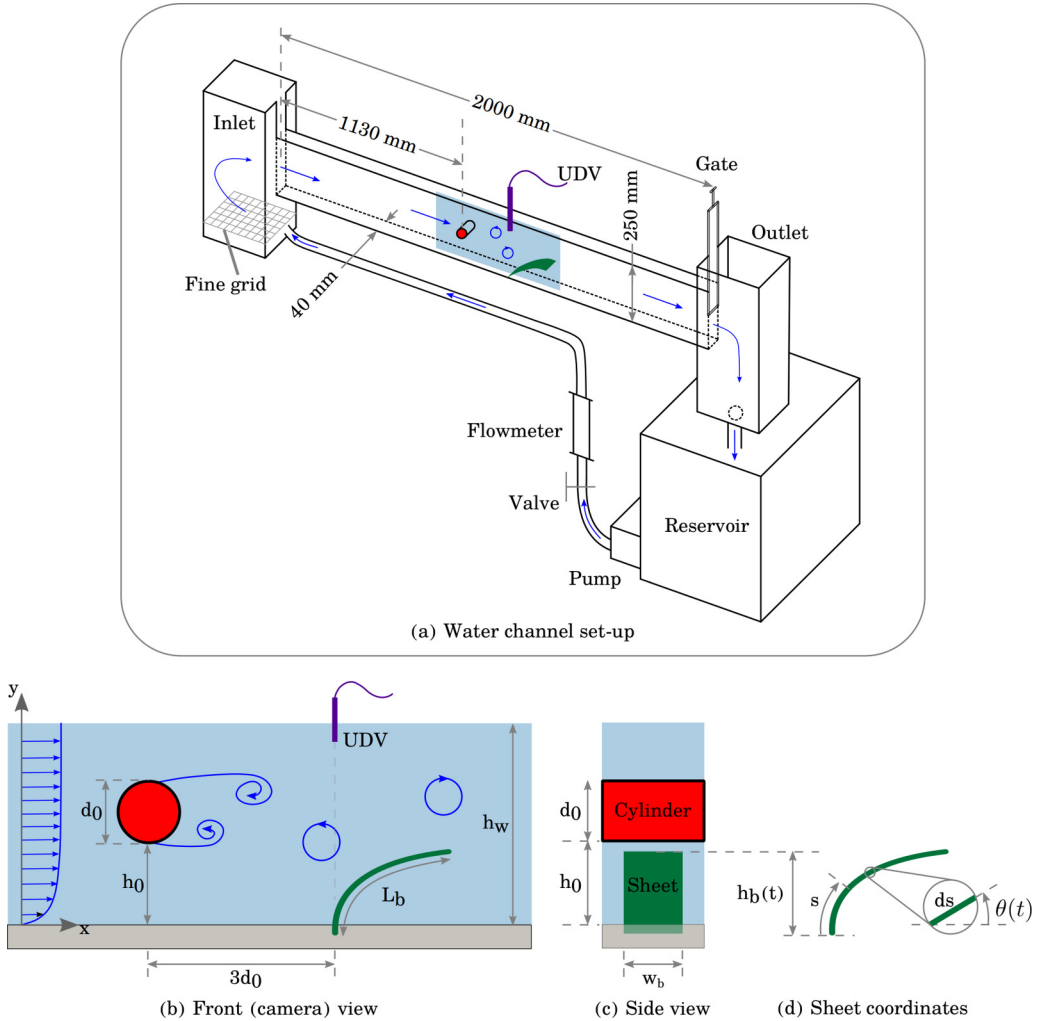


FIG. 1. Schematic view of (a) the two-meter long water channel along with (b) top and (c) front view, illustrating (d) the curvilinear coordinates for a bent sheet. The cylindrical obstacle is set up such that its base coincides with the top of the sheet, in the absence of any flow.

uniform channel flow whose water height is kept identical throughout this work ($h_w = 22.1$ cm). Figures 1(b) and 1(c) illustrate this setup wherein the cylinder and the sheet are exposed to a uniform channel flow directly orthogonal to the sheet's section $L_b w_b$.

In the range of depth-averaged flow speed $U_0 = 2.2 - 8.8$ cm s^{-1} and diameters $d_0 = 10, 20, 40$ mm used here, the cylinder Reynolds number $Re_d = U_0 d_0 / \nu$ varies over a decade, between 236 and 3773. An ultrasonic Doppler velocimetry (UDV) is used to obtain vortex street characteristics at the center plane of the channel and at a fixed position downstream, equal to three times the cylinder diameter. The probe measures the instantaneous vertical velocity component in the water flow at an acquisition frequency of about 2 MHz for three minutes. The range of shedding frequency varies between 0.14 and 2.13 Hz as indicated in Table I (see also Supplemental Material [41] and references therein [42–44]).

Five different cases of low-density polyethylene (density $\rho_b = 920$ kg m^{-3} and mass ratio 0.93) sheets from GoodFellow Cambridge Limited are used in our experiments. A snap-off blade knife

TABLE I. Characteristics of Bénard-Kàrmàn vortices for a range of water speed $U_0 = 2.2 - 8.8 \text{ cm s}^{-1}$. The shedding frequencies were obtained using ultrasonic Doppler velocimetry (UDV). As compared to the cylinder Reynolds number $\text{Re}_d = U_0 d_0 / \nu$, the hydraulic Reynolds number $\text{Re}_h = U_0 D_h / \nu$ varies from 1730 to 6920, wherein the hydraulic diameter is $D_h = 4h_w w_c / (2h_w + w_c)$ and the water height $h_w = 22.1 \text{ cm}$ is kept constant for all experiments. The reduced frequency $u = f_v / f_n \gtrsim 1$ for all cases considered here, and also it increases almost as $C_y^{9/5}$ (not shown here).

d_0 (mm)	$U_0 d_0 / \nu$	f_v (Hz)	f_v / f_n
10	236 – 943	0.14 – 0.63	2 – 360
20	472 – 1886	0.28 – 1.26	1 – 210
40	943 – 3773	0.37 – 2.13	0.8 – 105

was used to cut large sheets to prepare long blades. This is a delicate task, especially for longer and thinner sheets, as the process often leads to some local plastic deformation at its edges. In addition, some defects were initially present in the sheets. See Table II for the sheet length L_b , the thickness e_b , and other physical properties. The sheet thickness is chosen to always be very small compared to all other dimensions. For the sake of simplicity, the gap between the sheet and the channel walls is taken to be narrow, so the force exerted by the channel flow on the sheet is predominantly due to profile drag. The Cauchy number

$$C_y = \frac{C_d \frac{1}{2} \rho U_0^2}{E} \left(\frac{L_b^3 w_b}{I} \right), \quad (1)$$

which expresses the ratio of the flow drag and the elastic restoring forces, is varied in wide a range between $O(1)$ and 10^5 . Here, U_0 is the depth-averaged flow speed, E is the Young's modulus, the second moment of inertia for a thin flexible sheet is taken as $I = w_b e_b^3 / 12$, and C_d is the profile drag coefficient of a thin flat plate perpendicular to the flow direction. Based on measurements from our previous work, namely, Barsu *et al.* [45, see Fig. 6(a)], $C_d = 6$ is taken throughout the present work.

An estimate for the natural frequency of a fixed-free cantilever beam in a fluid can be found in classical texts such as Refs. [13,46],

$$f_{ni} = a_i \sqrt{\frac{EI / w_b L_b^4}{\rho_b e_b + \pi C_M \rho w_b / 4}}, \quad (2)$$

where a_i is a nondimensional constant ($a_1 = 0.56$ and $a_2 = 3.5$ for the first-order and second-order natural frequencies, respectively) and C_M is the added mass coefficient. Note that this *natural*

TABLE II. Geometric and mechanical properties of low-density polyethylene sheets along with the range of related Cauchy numbers attained in this work. All sheets are less dense than water (density $\rho_b = 920 \text{ kg m}^{-3}$) and their width ($w_b = 15 \text{ mm}$) is kept constant throughout this work. The sheet ID also indicates their stiffness ratio given by L_b / e_b .

ID	L_b (mm)	e_b (mm)	E ($\times 10^6 \text{ Pa}$)	$C_y = \frac{C_d \frac{1}{2} \rho U^2}{E} \left(\frac{L_b^3 w_b}{I} \right)$	$B_a = \frac{\Delta \rho g e_b}{E} \left(\frac{L_b^3 w_b}{I} \right)$	f_{n1} (Hz)	Symbol
S442	84	0.19	210	5 – 88	0.55	0.286	\triangleleft
S1263	240	0.19	210	130 – 2000	12.8	0.035	\square
S1400	84	0.06	230	908 – 4200	8.3	0.042	\circ
S2000	200	0.10	250	2100 – 9800	32.1	0.018	\star
S4000	240	0.06	230	12500 – 98200	192.4	0.005	\diamond

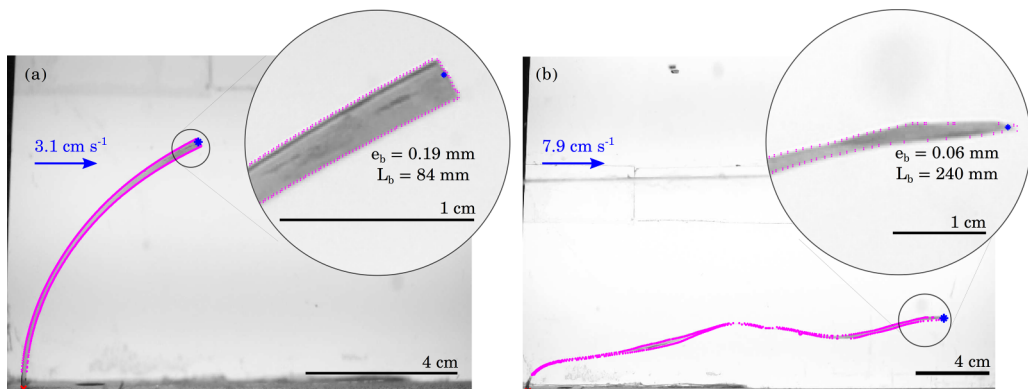


FIG. 2. Two examples showing the results of sheet edge detection via IMAGEJ with insets displaying a zoom on the tip of the sheet. (a) S442: $C_y = 11.3$, $Re_h = 2.5 \times 10^3$, $Re_d = 1.4 \times 10^3$ and (b) S4000: $C_y = 7.83 \times 10^4$, $Re_h = 6.2 \times 10^3$, $Re_d = 3.4 \times 10^3$. Here, dots (pink) show the detected sheet edge while an asterisk (blue) and a cross (red) each indicate the sheet's tip and foot, respectively.

frequency is usually attributed to beams in fluids that undergo small-amplitude vibrations and small deflections. Hence, such a frequency might not be relevant to long flexible sheets considered in this work since they exhibit large deflections. Also, these sheets are *pretensioned* due to the presence of a mean flow drag.

A high-resolution, full-frame digital camera (Sony $\alpha 7$) is used to image the vortex-forced oscillations of the flexible sheet at a rate of 25 images per second for a time period of seven to eight minutes (see Supplemental Material [41] for videos). The resulting images are analyzed using the open-source freeware IMAGEJ [47] and algorithms therein for brightness thresholding [48,49], edge detection, etc. Sample images and the corresponding edge detection (dots, pink) are shown in Figs. 2(a) and 2(b). Clearly, the contour of the sheet is well-detected. The sheet tip is taken as the center of the last identified sheet edge. This allows for well-resolved tip detection amplitudes in the order of a few tens of a millimeter.

In the following sections, all experimental results are presented in terms of the depth-averaged water speed across the time-averaged deflected sheet height \bar{h}_b . This speed is based on the classical *Coles* law for the channel velocity profile $U(y)$, so $U_h \bar{h}_b = \int_0^{\bar{h}_b} U(y) dy$. Each symbol, namely, \triangleleft , \square , \circ , \star , and \diamond , represents different sheets of increasing stiffness ratio (L_b/e_b), respectively, provided in Table II.

III. TIME-AVERAGED SHEET RECONFIGURATION

In the absence of a vortex street, at any chosen flow rate and constant water height, a sheet bends in the flow direction and exhibits a deflected height $h_b < L_b$. This leads to the well-known drag reduction since the profile drag force experienced by a flexible sheet $F_d = C_d \frac{1}{2} \rho U^2 h_b w_b$ is smaller than that experienced by the same sheet if it was rigid (here, C_d is the sheet drag coefficient). Such a drag reduction is often quantified by expressing the so-called *static* reconfiguration number $\mathcal{R} = h_b/L_b$ as a function of the flow speed U_0 and the so-called Vogel number [17] i.e., $h_b/L_b \sim U_0^\mathcal{V}$. Thereby, the profile drag can be written as a power law

$$F_d \propto \frac{1}{2} \rho U_0^{2+\mathcal{V}} A_f,$$

where $A_f = L_b w_b$ is the undeformed sheet frontal area. Then, drag reduction by reconfiguration is observed if the Vogel number is $\mathcal{V} < 0$. For example, the Vogel number $\mathcal{V} = -2/3$ for long thin blades which are anchored to the flow bed at its one end [20]. While the reconfiguration number expresses the frontal area reduction, a more appropriate way to estimate drag reduction by

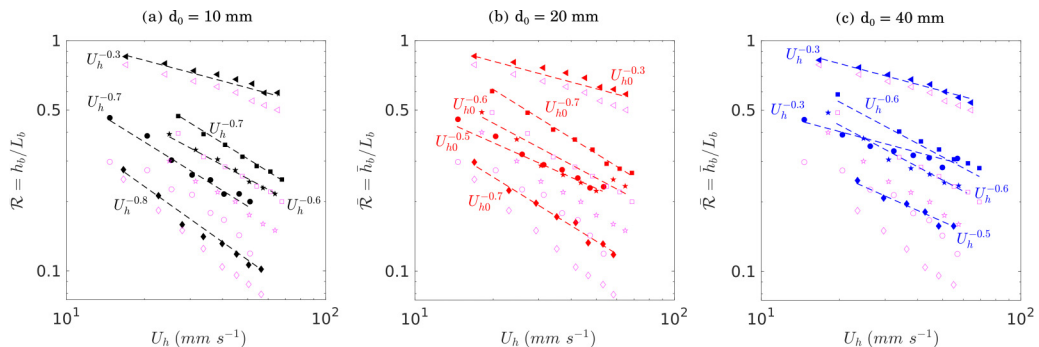


FIG. 3. Time-averaged sheet reconfiguration $\bar{\mathcal{R}}_b = \bar{h}_b/L_b$ in the presence of Bénard-Kármán vortices as a function of the depth-averaged water speed across the sheet height (U_h). All symbols indicate different stiffness ratio (L_b/e_b) as given in Table II. Open symbols represent data for the same cases as filled symbols but in the absence of an upstream cylinder.

reconfiguration is to compute the effective blade length proposed by Ref. [50]. Such a length also includes the streamlining effect due to bending at the foot of the sheet. For the sake of simplicity, we consider the reconfiguration number which only accounts for area reduction. This provides an upper bound for drag reduction by reconfiguration as well [50].

In this context, Fig. 3 displays the *dynamic* reconfiguration number $\bar{\mathcal{R}} = \bar{h}_b/L_b$ against water speed for each of the five sheets in our study. Here, each column corresponds to data for a particular cylinder diameter d_0 . Reconfiguration data in the absence of any upstream cylinder is also presented in each figure for comparison (open symbols; light magenta). We observe that the average reconfiguration number is always lesser than unity and the related time-averaged sheet deflection can be as small as one-tenth of its length. Furthermore, in all cases corresponding to a fixed L_b/e_b , $\bar{\mathcal{R}}$ decreases when the flow speed increases. So, the frontal area of a given sheet that is exposed to the incoming flow decreases with speed, leading to an average drag reduction by reconfiguration. By comparing each filled symbol in Fig. 3 with its corresponding open symbol, we note that $\bar{\mathcal{R}} = \bar{h}_b/L_b$ always falls above the values of $\mathcal{R}_0 = h_0/L_b$. So, the time-averaged sheet deflection at a given speed is systematically bigger than its counterpart in the case of a flexible sheet free of an upstream cylinder. We refer to this as a lift-up effect. It is observed to be more pronounced for bigger cylinder d_0 and also at higher water speeds U_h . However, at a fixed d_0 and U_h , the influence of the sheet's stiffness ratio L_b/e_b on the lift-up effect is not straightforward.

Direct measurement of drag force is not possible in our experimental setup. However, a measure of the average drag reduction during the vortex-forced motion of thin flexible sheets can be inferred from Fig. 3 by estimating the so-called Vogel number \mathcal{V} . As is common for the case of a steady flow over a flexible sheet, we associate a power law $\bar{h}_b/L_b \sim U_h^\mathcal{V}$ and deduce a Vogel number \mathcal{V} for each stiffness ratio (L_b/e_b). Except for the sheet with the smallest stiffness, all the other sheets present a Vogel number $\mathcal{V} \approx -0.6 \pm 0.1$. Note that similar values were previously obtained in the same water channel, but for submerged artificial canopies of Kevlar sheets undergoing *static* reconfiguration [45, Fig. 4(a)]. We observe that the Vogel parameter is almost independent of cylinder diameter d_0 for sheets S442, S1263, and S1400. For more flexible blades (S2000 and S4000), a decrease in the Vogel parameter with increasing d_0 is observed. This suggests that vortices perhaps hinder the time-averaged drag reduction by reconfiguration of flow-bent flexible structures. In addition, this effect seems to be stronger for more flexible blades and bigger vortices. It is now well-established that a bending beam, accounting for the *local* flow drag and the Archimedes force due to buoyancy, provides a satisfactory mechanical model for *static* reconfiguration of flexible sheets [45,50–52]. If s is the curvilinear coordinate along the sheet and $\theta(s)$ the *local* sheet deflection

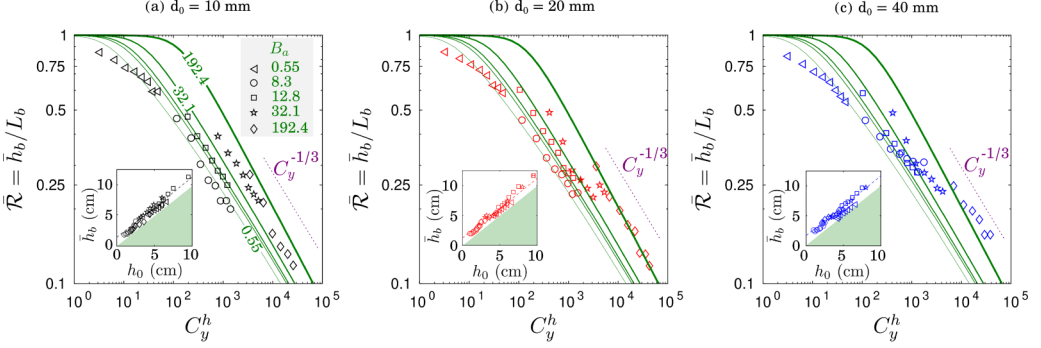


FIG. 4. Time-averaged sheet reconfiguration $\bar{\mathcal{R}}_b = \bar{h}_b/L_b$ expressed in terms of the *local* Cauchy number $C_y^h = 12(C_d \frac{1}{2} \rho U_h^2 / E)(L_b^3 / e_b^3)$ and compared with continuous lines (green) as obtained from the bending beam model [Eq. (4)]. The inset compares the average sheet deflection against the corresponding cylinder's vertical position.

as represented in Fig. 1(d), the restoring bending moment $M(s)$ at any arbitrary distance s from the sheet's foot should be given by

$$EI \frac{d\theta}{ds} = \int_s^{L_b} (x(\xi) - x(s)) dF_A - \int_s^{L_b} (\xi - s) dF_D, \quad (3)$$

where $dF_A = \Delta \rho g (e_b w_b d\xi)$ is the *local* Archimedes force and $dF_D = C_d \frac{1}{2} \rho U^2 \sin^2(\theta(\xi)) dA_f$ is the normal component of the *local* profile drag, with $\Delta \rho = \rho - \rho_b$ the density difference between the fluid and the sheet and $dA_f = w_b d\xi$ the *local* frontal area of the *reconfigured* sheet.¹ The above equation can be further simplified by taking both $U(s) \equiv U_0$ and EI to be invariant across the sheet so

$$\frac{d^3\theta}{d\tilde{s}^3} = B_a \left(\sin\theta(1 - \tilde{s}) \frac{d\theta}{d\tilde{s}} + \cos\theta \right) - C_y \sin^2\theta, \quad (4)$$

where $\tilde{s} = s/L_b \in [0, 1]$ is the nondimensional curvilinear coordinate, $B_a = \Delta \rho g w_b e_b L_b^3 / EI$ is the so-called Buoyancy number, and $C_y = C_d \rho w_b L_b^3 U_0^2 / 2EI$ is the Cauchy number. The typical values for these nondimensional numbers are also provided in Table II. This model equation can be readily solved by applying the boundary conditions at the sheet extremities $\theta = \pi/2$ and $d\theta/ds = d^2\theta/ds^2 = 0$, for $\tilde{s} = 0$ and $\tilde{s} = 1$, respectively.

Let us now investigate the *dynamic* reconfiguration number as a function of Cauchy number, as provided in Fig. 4. As before, we use the depth-averaged water speed U_h across the time-averaged deflected sheet height \bar{h}_b to express data in terms of the *local* Cauchy number $C_y^h = 12C_d \frac{1}{2} \rho U_h^2 / E(L_b / e_b)^3$. Symbols represent experiments and continuous lines are computed from the bending beam model in Eq. (4) at each various Cauchy and Buoyancy number. For a given blade, say, for instance, S442 as represented by \triangleleft , as C_y increases, the sheet reconfiguration decreases monotonically. However, at a fixed Cauchy number C_y , reconfiguration data from all sheets do not collapse on a single master curve. A closer observation reveals that this is due to Buoyancy, which tends to increase the reconfiguration for sheets of larger Buoyancy number $B_a = 12\Delta \rho g e_b / E(L_b / e_b)^3$. Despite the fact that the above-mentioned bending beam model is only valid for the case of a *static* reconfiguration under a steady uniform flow, it predicts the trend with

¹Note that the effect of the sheet's curvature on the bending moment due to the drag force and the tensile stress along the length of the sheet are neglected for simplicity.

the Cauchy number and also the Buoyancy number for all cases. It displays a reasonable agreement for $C_y > O(1)$.

Furthermore, Fig. 5 compares the time-averaged sheet shape with that computed via the bending beam model [Eq. (4)]. Note that the model provides a satisfactory estimate despite the strong approximations such as uniform, steady flow across the sheet. As already mentioned in Sec. II, defects were often present in the biaxially oriented thin polyethylene sheets. This is visible for the most flexible blade in our study, namely, S4000 at the smallest speed ($U_0 = 22 \text{ mm s}^{-1}$, red color). Nevertheless, the influence of the nonuniform velocity profile is perhaps more significant in discrepancies between the model and experiments than any initial plastic deformation.

Finally, an estimation for these differences between experimental data and the steady flow model can be obtained by analyzing the lift-up effect. As observed in Figs. 3 and 4 (insets), the sheet deflection height h_b/L_b in the absence of vortices is smaller than the *dynamic* reconfiguration $\overline{\mathcal{R}} = \bar{h}_b/L_b$. Also, the lift-up effect is more pronounced as the diameter of the upstream cylinder increases, and it arises from the presence of an upstream cylinder, which leads to an oscillating velocity field in the vicinity of the sheet's tip, and a velocity defect in the longitudinal component of the mean flow downstream. So, for some average velocity defect $\overline{\Delta u} < 0$, we deduce an estimate from the well-established power law $h_0/L_b \sim U_h^\mathcal{V}$ for *static* reconfiguration to obtain for its *dynamic* counterpart as $\bar{h}_b \sim h_0(1 + \mathcal{V}\overline{\Delta u}_v/U_h)$. Suppose that this defect occurs in the sheet tip's neighborhood of size l_v . Since the cylinder's vertical position is fixed at h_0 for each experiment, we then have $\overline{\Delta u} \sim -U_h l_v/h_0$, up to a first-order correction of the mean flow U_h . Therefore, it is expected that $\bar{h}_b \sim h_0 - \mathcal{V}l_v$, with $\mathcal{V} < 0$. Let us now compare this relationship with plots of \bar{h}_b against h_0 , as given in the insets of Fig. 4. We note that the general trend of data points reasonably agrees with the relation $\bar{h}_b \sim h_0 - \mathcal{V}l_v$. Hence, the lift-up effect in *dynamic* reconfiguration could be understood as a consequence of the presence of cylinder wake. It can also be inferred that the length scale l_v depends on the cylinder diameter d_0 . Nonetheless, the decrease in the Vogel exponent for more flexible sheets cannot be completely explained via a small-velocity defect argument as here. This phenomenon is perhaps analogous to a time-averaged reconfiguration in wave-induced oscillations of submerged flexible structures [53–55]. They obtain a scaling law for both the effective blade length [50] and the deflected height is found to be $\bar{h}_b/L_b \sim C_y^{-1/4}$, with a proportionality constant which depends on the ratio of the blade length and the wave amplitude. Thus, our results suggest that the *dynamic* reconfiguration tends towards wave-induced mean blade reconfiguration when the cylinder diameter increases.

IV. SHEET OSCILLATION AMPLITUDE

If $(x_b(t), y_b(t))$ represent the sheet tip's instantaneous position and (\bar{x}_b, \bar{y}_b) their time average, then let us define the tip oscillation amplitude based on the standard deviation, as in

$$\delta_b \equiv 2\sqrt{\overline{(x_b(t) - \bar{x}_b)^2} + \overline{(y_b(t) - \bar{y}_b)^2}}, \quad (5)$$

where $\bar{\cdot}$ represents mean values. Figure 6 presents such an amplitude as a function of the local water speed $U_{h_0} = U(y = h_0)$ computed from the *Coles law* channel velocity profile times the cylinder diameter d_0 . Also, $U_{h_0}d_0$ is proportional to the *local* cylinder Reynolds number. Each open symbol corresponds to a stiffness ratio as given in Table II and other symbols \cdot , $+$, and \times indicate cylinder diameters $d_0 = 10, 20$ and 40 mm , respectively. For a given sheet and cylinder, the tip fluctuation amplitude increases proportionally with the local water speed U_{h_0} . Now, as the cylinder diameter is varied, similar behaviors are again observed but the tip amplitudes δ_b are smaller for smaller diameters. In addition, sheets with higher stiffness ratio L_b/e_b show increasingly larger amplitudes while data for sheets with approximately the same stiffness ratio, as in S1263 (\square) and S1400 (\circ) fall almost on the same linear trend line. In general, it is inferred from these observations that the tip amplitude not only increases with the sheet stiffness ratio L_b/e_b but also with $U_{h_0}d_0$.

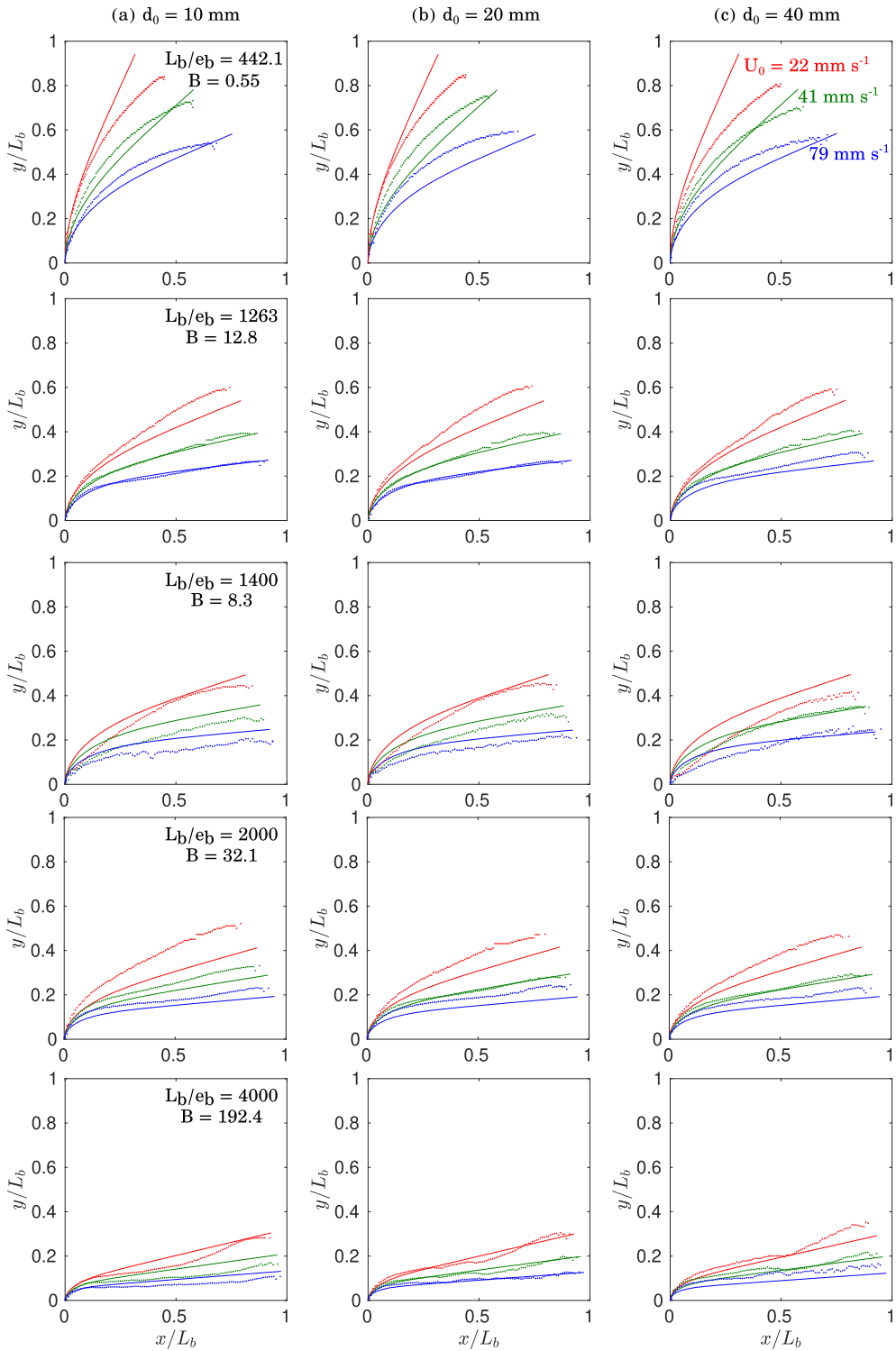


FIG. 5. Typical time-averaged sheet shape from experiments (dots) as compared to bending beam model (continuous lines), allowing for the effect of buoyancy in a steady, uniform channel flow [Eq. (4)].

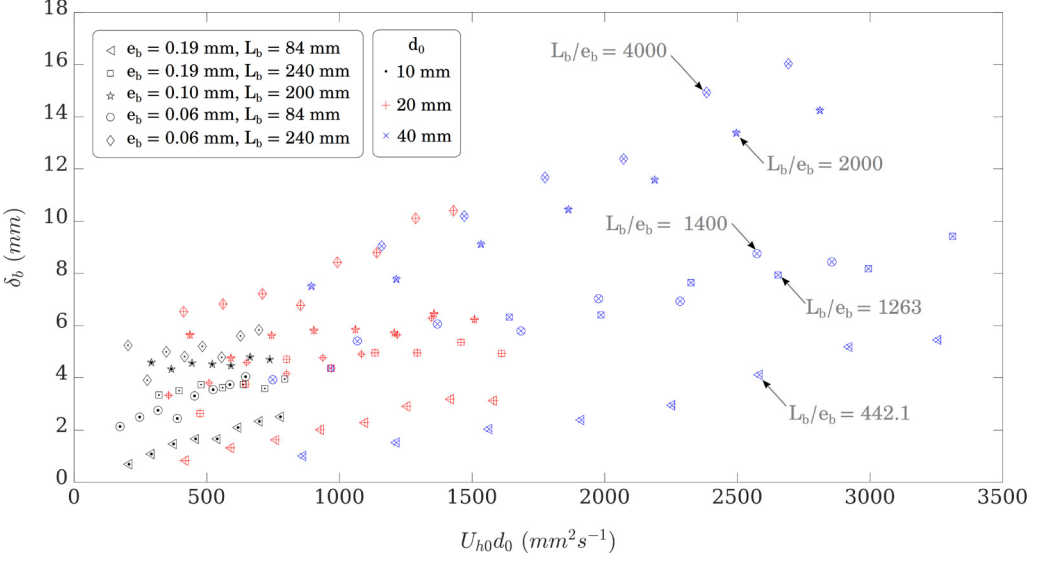


FIG. 6. Tip oscillation amplitude δ_b as a function of an equivalent vortex circulation $U_{h0}d_0$, where U_{h0} is the water speed at the cylinder center.

A simple model can be derived if we decompose the total work done by the vortex-laden flow on the flexible sheet into two distinct parts: (i) the steady component of the flow leads to the average angular position, say $\bar{\xi}$, and (ii) the periodic interaction between the vortices and spring-supported flat plate results in torsional vibrations of the spring, and hence the plate's angular position $\xi(t)$. Then, locally, the average profile drag-induced moment should be balanced by the average restoring moment in the deflected sheet $EId\theta/ds$, where $d\theta/ds$ is the sheet's local curvature ($1/R_c$). As already observed in Sec. III, at very large Cauchy number which compares drag force against the elastic restoring force, $\bar{h}_b \ll L_b$, and hence it can be safely assumed that $EId\theta/ds \approx EI/\bar{h}_b$, since R_c is approximately equal to the time-averaged sheet deflection \bar{h}_b (see Fig. 7). And so, we obtain

$$\begin{aligned} \frac{EI}{\bar{h}_b} &\sim \left(C_d \frac{1}{2} \rho U_0^2 w_b \bar{h}_b \right) \times \bar{h}_b, \\ \Rightarrow \frac{\bar{h}_b}{L_b} &\sim C_y^{-1/3}, \end{aligned} \quad (6)$$

a result analogous to the well-known scaling for the *static* reconfiguration number [20,21] that leads to drag reduction in flexible plates. When $C_y \ll 1$, on the other hand, $\bar{h}_b \approx L_b$. Note that the experimental data provided in the previous section, as in Fig. 3, match fairly well with the above large-Cauchy number scaling law, irrespective of Buoyancy number. In general, the above result could also be expressed as $\bar{h}_b/L_b \sim C_y^{\mathcal{V}/2}$, where the Vogel number $\mathcal{V} = -2/3$ at $C_y \gg 1$ [20].

Furthermore, we propose that the vibrational energy of the sheet is solely taken from Bénard-Kármán vortices at some rate depending on the characteristics of the incoming unsteady flow, and during some timescale proportional to the shedding period $1/f_v$. Therefore, for the toy model, we have

$$\frac{1}{2} \mathcal{K} \left(\frac{\delta_b}{L_b} \right)^2 \sim \left(\frac{1}{2} \rho U_0^3 w_b d_v \right) \frac{1}{f_v}, \quad (7)$$

where the left-hand side is the vibrational energy of the torsional spring and the right-hand side is the product of *local* kinetic energy transfer rate, taken here as proportional to $1/2 \rho U_0^3 w_b d_v$, and

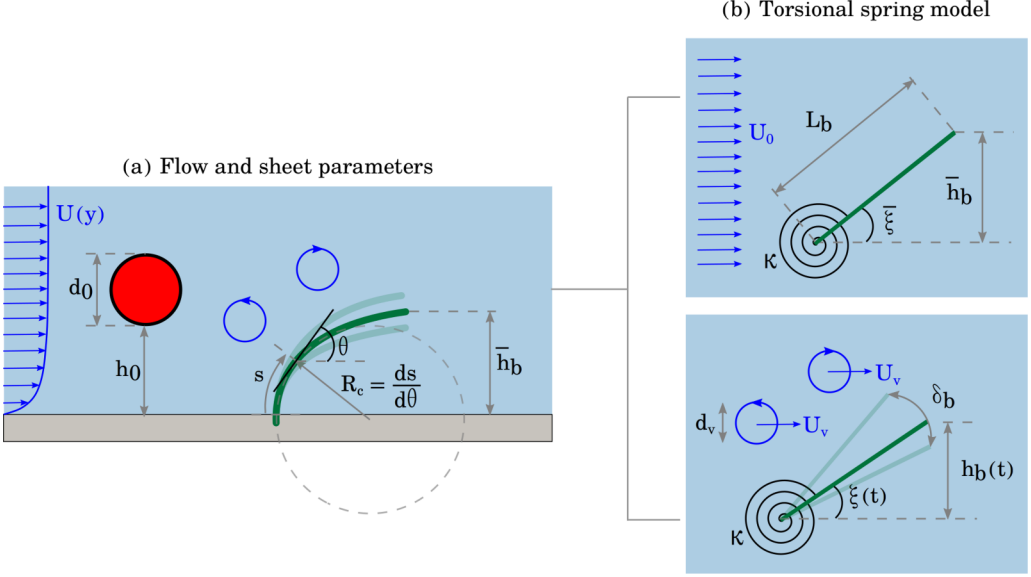


FIG. 7. Schematic of the flow and sheet parameters along with that of the torsional spring model.

the typical timescale during which the transfer periodically takes place, i.e., $1/f_v$. Here, d_v is some characteristic length scale of Bénard-Karman vortices. Also, in the above expression, the stiffness \mathcal{K} of the *pretensioned* torsional spring can be ascertained from the equilibrium condition that $\mathcal{K}\bar{\xi} \equiv EId\theta/ds \approx EI/\bar{h}_b$, with $\bar{\xi} \approx \bar{h}_b/L_b$ when $Ca \gg 1$ since $\bar{h}_b \ll L_b$. Now, in terms of the Vogel number $\mathcal{V} = -2/3$ at $C_y \gg 1$ or $\mathcal{V} = 0$ at $C_y \ll 1$. By admitting that the *dynamic* reconfiguration number is $\bar{h}_b/L_b \sim C_y^{\mathcal{V}/2}$, it can be deduced that $\mathcal{K} \sim (EI/L_b)C_y^{-\mathcal{V}}$. Thereafter, the expression Eq. (7) leads to

$$\left(\frac{\delta_b}{L_b}\right)^2 \sim \left(\frac{\rho U_0^2 w_b L_b}{EI}\right) \left(\frac{U_0 d_v}{f_v}\right) C_y^{\mathcal{V}}, \quad (8)$$

$$\Rightarrow \frac{\delta_b}{d_v} \sim C_y^n St_v^{-1/2}, \quad (9)$$

where $St_v = f_v d_v / U_0$ is the Strouhal number based on a typical size of the eddies, and $n \equiv (1 + \mathcal{V})/2 = 1/6$ or, respectively, $1/2$, for sufficiently large Cauchy numbers $C_y \gg 1$ or otherwise.

Figure 8 presents the same tip amplitude data given in Fig. 6 but, instead, they are rescaled in terms of the experimentally obtained values of the Strouhal number St_v , the depth-averaged velocity U_0 , and the characteristic vortex length scale d_v . Note that the typical eddy scale d_v , as provided in Fig. 8 (inset), is estimated via particle image velocimetry (PIV) measurements using standard recommendations as in Ref. [56] (for more, see Supplemental Material [41]). Clearly, experimental data ranging over all Cauchy numbers investigated here are regrouped around two distinct trend lines, namely, $C_y^{1/2}$ and $C_y^{1/6}$, each corresponding to the case of moderately small and large Cauchy numbers, respectively, as expressed by the relation Eq. (9). In the former, the sheet reconfiguration is sufficiently small, and so it represents vibration of a rigid sheet forced by a vortex street, whereas, in the latter case, sheets can be considered to be flexible. These results strongly suggest that the torsional spring model contains the essential mechanism to explain the observed vortex-forced vibration of thin sheets. They also imply that, analogous to drag reduction via reconfiguration under an external flow, a flexible sheet experiences a smaller vibration amplitude compared to that of a rigid sheet when excited by a Bénard-Kàrmàn vortex street. Finally, it is pointed out that the expression the *dynamic* reconfiguration number may not, in general, be given by $\bar{h}_b/L_b \sim C_y^{\mathcal{V}/2}$,

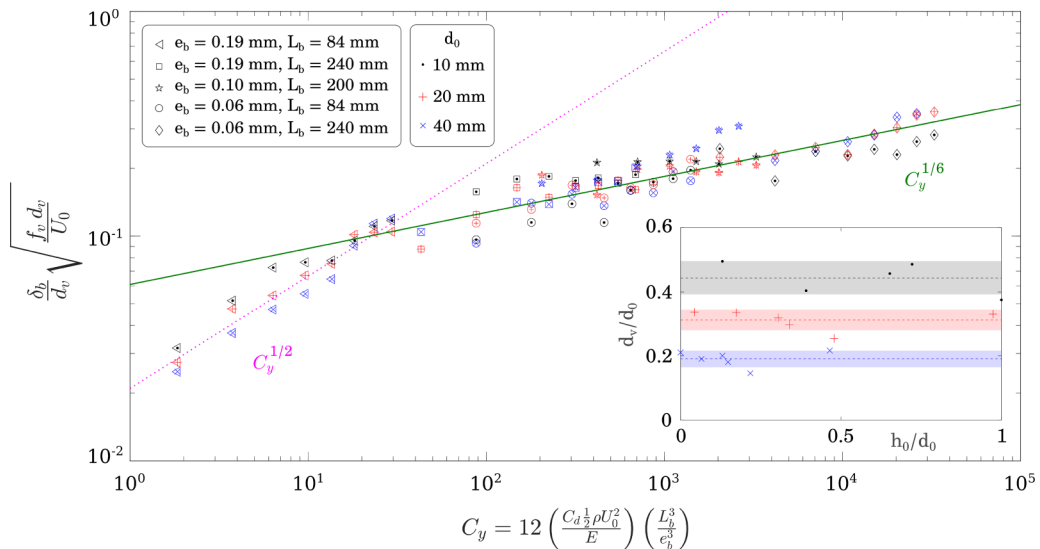


FIG. 8. All data from Fig. 6 are expressed in terms of the *rescaled* oscillation amplitude of the sheet's free end δ_b/d_0 as given by the relationship Eq. (9) versus the Cauchy number $C_y = 12(C_d^{1/2} \rho U_0^2/E)(L_b^3/e_b^3)$. Two distinct regimes are visible here.

and this expression is valid only for either sufficiently small, or large, Cauchy numbers [57]. In addition, the reconfiguration number should also depend on the Buoyancy number for intermediate Cauchy numbers [50]. So, it is possible that the transition between the two regimes of vortex-forced oscillations may perhaps not be as abrupt as in our experiments.

V. SHEET BEATING FREQUENCY

The time evolution of tip response of a sheet S442 subject to Bénard-Kármán vortices shed by a cylinder ($d_0 = 40$ mm) at the lowest and highest water speed is considered in this section, respectively, as displayed in Figs. 9(a) and 9(b). In Fig. 9(a), at $U_0 = 3.1$ cm s⁻¹, both vertical and horizontal oscillations are of the same order of magnitude and they are also synchronous. As the speed increases to $U_0 = 7.9$ cm s⁻¹, y fluctuations present an almost proportionally increased *back-and-forth* amplitude while x fluctuations are much smaller in magnitude. Clearly, x -tip detection seems to be not so robust for this case. Their corresponding power spectral densities are provided on the immediate right of the same figures. Here, arrows are used to indicate the forcing frequency (vortex shedding) $f_v = 0.56$ Hz and the first natural frequency $f_{n1} = 0.29$ Hz, respectively. Clearly, the sheet tip oscillates at the vortex shedding frequency for these two cases.

The above examples correspond to the sheet for which the relevant Cauchy numbers ($C_y = 5 - 88$) are the smallest. In comparison, Fig. 9(c) gives the tip fluctuations for S4000, at one of the largest Cauchy numbers ($C_y = 9 \times 10^4$). This sheet exhibits large amplitude oscillations in the vertical direction as big as the cylinder diameter $d_0 = 40$ mm while the horizontal oscillations remain small ($\lesssim 4$ mm) as before. The corresponding spectra of the vertical tip position presents a peak at 0.15 Hz, along with a smaller second peak at the vortex shedding frequency $f_v = 0.55$ Hz. Qualitatively similar temporal characteristics are observed for the sheet tip when diameter d_0 is decreased. For example, Fig. 9(d) provides typical data at $d_0 = 10$ mm to be compared with its equivalent case at the same water speed and sheet physical properties given in Fig. 9(c). First, the vertical oscillations are diminished almost in proportions to the diameter ratio. Second, the power spectral density neither presents a peak at the vortex shedding frequency $f_v = 0.55$ Hz nor at the sheet natural frequency $f_v = 5 \times 10^{-3}$ Hz. Instead, the peak occurs at almost the same frequency

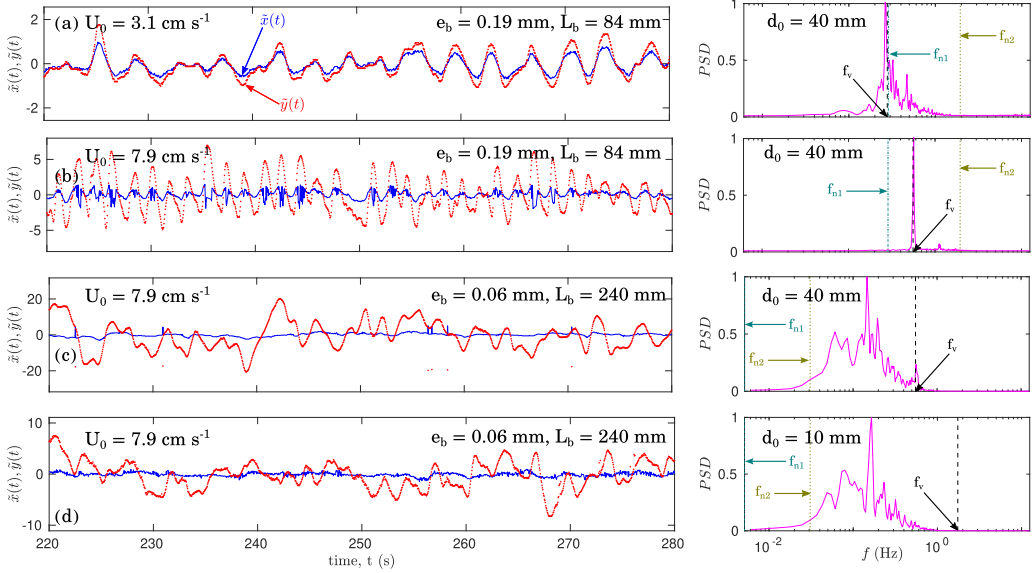


FIG. 9. Left: Blade tip oscillations (in mm) of the stiffest sheet S442 at different depth-averaged water speed (a) $U_0 = 3.1 \text{ cm s}^{-1}$, (b) $U_0 = 7.9 \text{ cm s}^{-1}$ as compared with the most flexible sheet S4000 at (c) $U_0 = 7.9 \text{ cm s}^{-1}$ due to vortices shed by a cylinder of diameter $d_0 = 40 \text{ mm}$. (d) Same as (c) but for $d_0 = 10 \text{ mm}$. Right: Power spectral density of the sheet tip's vertical fluctuations. Arrows indicate various frequencies, namely, the vortex-shedding frequency (f_v) and the first two sheet's natural frequencies (f_{n1} and f_{n2}).

($0.16 \text{ Hz} < f_v$) as for the case with the larger diameter $d_0 = 40 \text{ mm}$. In fact, this peak is much closer to the flat-plate shedding frequency based on the average-deflected-height of the sheet, i.e., $0.145U_h/\bar{h}_b = 0.2$ for these cases. In summary, the peak-normalized power spectra suggests that the tip motion in the y direction oscillates either at the vortex shedding frequency f_v or at a different frequency lesser than f_v when d_0 decreases or L_b/e_b increases.

Figure 10 (top) displays a color plot of the power spectral density of the UDV-measured, instantaneous vertical velocity at the cylinder midspan and at a distance $3d_0$ downstream the cylinder wake. As already mentioned, UDV measurements were acquired at 2 MHz during 3 min. Colors, from bright yellow to black, represent the normalized spectra of the y component velocity field across the cylinder diameter. Here, the spectra at each y coordinate ($y \in [h_0, h_0 + d_0]$) is first computed and then an average in the discrete Fourier space is taken to obtain the normalized spectra. The latter presents a maximum [bright yellow, in Fig. 10 (top)] at a frequency f which is, by definition, equal to the vortex shedding frequency f_v .

Similarly, Fig. 10 (bottom) presents the power spectral density for the sheet-tip $y_b(t)$. For the sake of comparison, the x axis is kept the same as just before. Therefore, this figure illustrates the energy content of the sheet-tip oscillation for each forcing frequency, equal to the shedding frequency of the Bénard-Kármán vortices f_v . Note that the sheet tip position spectra is not quite the same as the y -component velocity power spectra discussed just before. Clearly, there are many cases where the power spectrum is wide for a fixed f_v . It is thereby inferred that the sheet's vibrational energy is distributed across different frequencies and the dominant frequency f_b varies from case to case. Nonetheless, the dominant frequency of sheet tip fluctuations is observed, in general, to be lower than the vortex shedding frequency f_v . Also, a second peak is often visible for some cases in Fig. 10 (bottom).

To further elucidate the distribution of vibrational energy in the sheet-tip vertical motion, Fig. 11 provides a few dominant tip frequencies f_b , i.e., those frequencies corresponding to the prominent

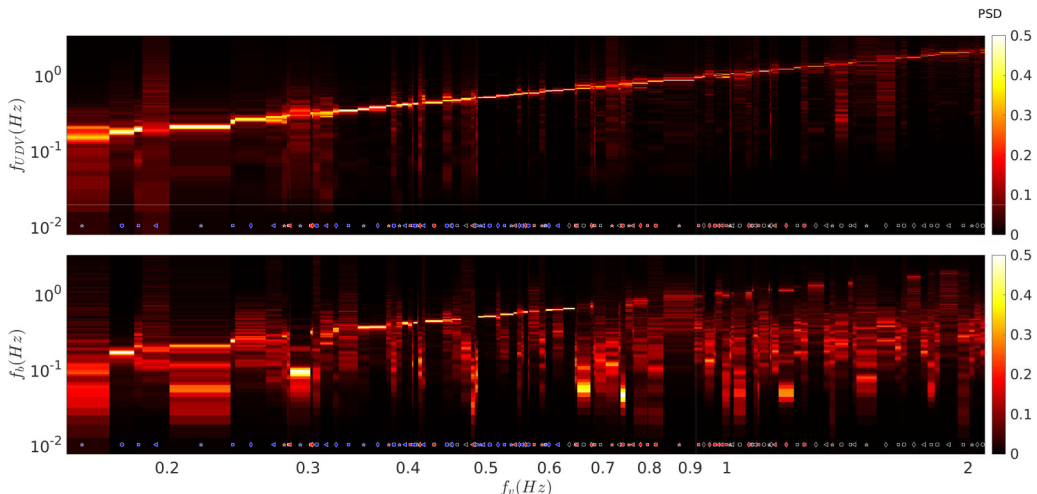


FIG. 10. Power spectral density for all experimental cases as a function of the forcing frequency f_v , corresponding to imposed periodic shedding of Bénard-Kàrmàn vortices. The frequency content of the (top) vertical velocity behind the cylinder, as measured using an UDV and (bottom) vertical fluctuations of the sheet's free end. Dashed line is given simply to show the trend while symbols are provided for the sake of reference only (see Fig. 8 for the corresponding sheet physical properties).

peaks in the corresponding power spectral density, for various imposed vortex shedding frequencies. The size of the data points are proportional to the normalized power spectra. In this figure, data in each row corresponds to single sheet characteristics, in the ascending order of the sheet stiffness ratio L_b/e_b while each column denotes data from experiments with the same cylinder diameter d_0 . The cylinder diameter d_0 increases from left to right. Here, the continuous line (green) provided to indicate the cases when $f_b = f_v$, i.e., the cases where the observed beating frequency of the sheet is equal to the forcing frequency due to Bénard-Kàrmàn vortices. Now it can be inferred from the data displayed in the last column, for experiments with the largest cylinder ($d_0 = 40$ mm), that the dominant frequency in the sheet-tip fluctuations is simply equal to the forcing frequency f_v , irrespective of the Cauchy number $C_y = 12(C_d \frac{1}{2} \rho U^2 / E)(L_b^3 / e_b^3)$. This is in contrast with the case when $d_0 = 10$ mm, wherein $f_b < f_v$ for all sheets and multiple prominent peaks in the power spectra of the tip's vertical fluctuation $y - \bar{y}_b(t)$. However, for some cases, namely, S442 and S1263, the prominent frequencies are about the first or second natural sheet frequency, respectively, as given by Eq. (2). Whereas, for the other cases, the data is scatter around the dashed line (blue), which denotes the expression $f_h = 0.145U_0/\bar{h}_b$, the flat-plate shedding frequency [11] based on the sheet deflected height \bar{h}_b , as known from the *dynamic* sheet reconfiguration. We also observe similar dynamical regimes for the intermediate cylinder size $d_0 = 20$ mm: (i) For the most rigid sheet S442 and for $C_y < 20$, the dominant blade frequency is seen to be the forcing frequency f_v , with a few dominant peaks either at the sheet's first natural frequency f_{n1} . (ii) For the most flexible sheets, namely, S2000 and S4000 and for $C_y > 10^3$, the sheets display oscillations at the vortex shedding frequency of an inclined flat plate given by $f_h = 0.145U_0/\bar{h}_b$. (iii) For moderate stiffness ratio and Cauchy numbers, the sheet oscillates either at one of its natural frequencies which is close to the forcing frequency f_v or at the inclined plate-shedding frequency f_h . Finally, it is pointed out here that no conclusive evidence for a critical Cauchy number nor a critical length scale for the vortices is observed in these data. Nonetheless, these observations strongly suggest that, in general, there is a transition from the forced-vortex-synchronous sheet-tip oscillation regime ($f_b = f_v$) to either a regime wherein the sheet-tip oscillations resemble the classical lock-in mode or a regime wherein the tip vibrations are

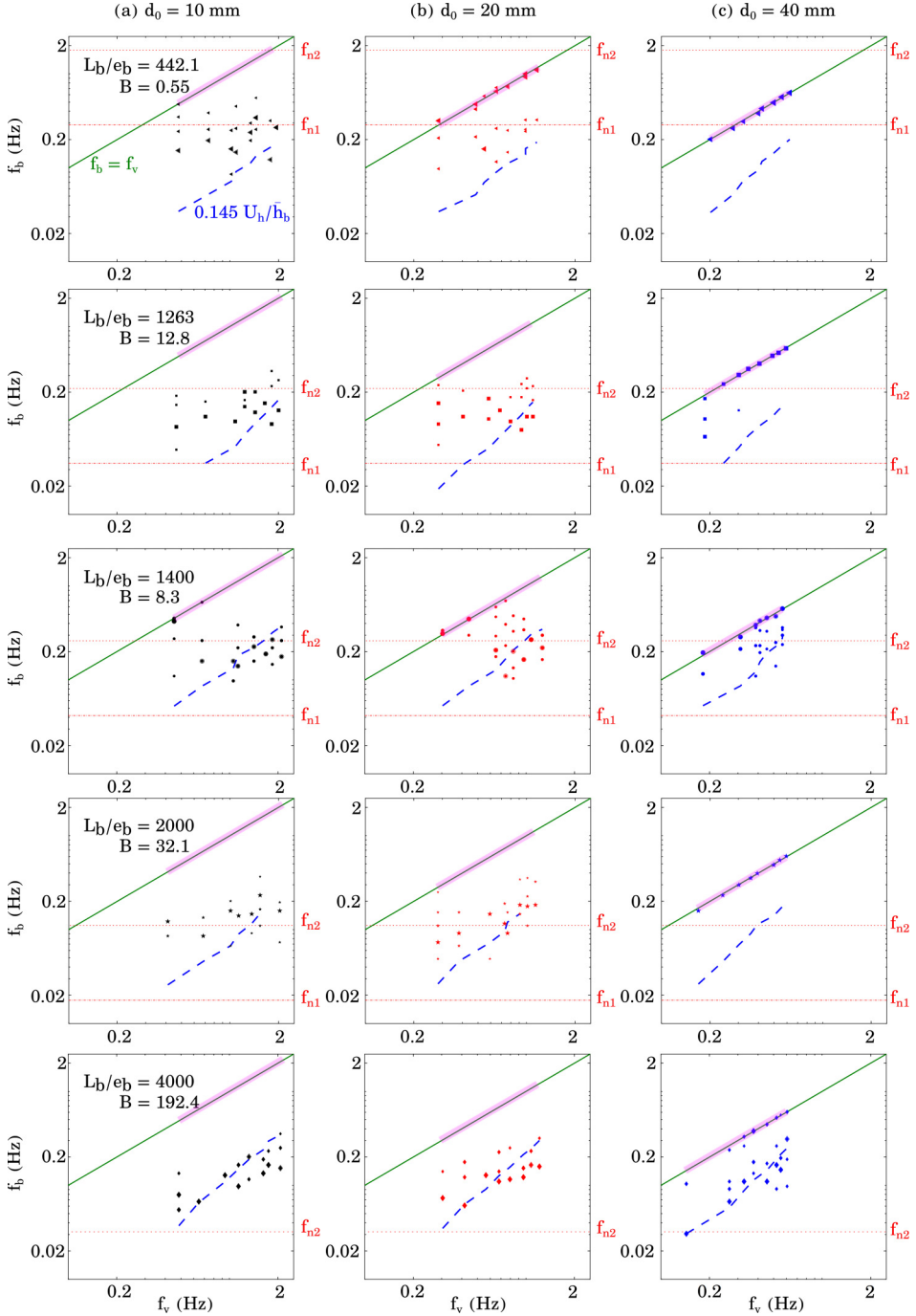


FIG. 11. A detailed view of the measured blade peak frequency as a function of the vortex shedding frequency f_v . Symbols denote the same cases as in Fig. 6 while symbol size at each forcing frequency f_v is proportional to the normalized power spectral density. Here, the continuous line (—) represents $f_b = f_v$ while the dot-dash line (· · ·) and the dotted line (· · ·) indicate the sheet's first and second natural frequencies f_{n1} and f_{n2} , respectively, and (— · —) is the flat-plate shedding frequency based on the sheet *deflected* height $f_h = 0.145 U_h / \bar{h}_b$. Also, in each case, pink bands indicate the forcing frequency range.

induced by its wake characteristics, and the transition between these dynamical oscillation modes should depend on the relative size of the Bénard-Kàrmàn vortices and the stiffness ratio.

VI. CONCLUSIONS

The role of vortical structures in a transverse water flow on the flow-induced reconfiguration and vibration of a thin flexible sheet fixed to the floor at one end are experimentally investigated. Sheets of varying lengths and thicknesses ($L_b = 84 - 240$ mm; $e_b = 0.06 - 0.19$ mm) and three different cylinder diameters $d_0 = 10, 20,$ and 40 mm are used for this purpose. Each experiment consists of rigidly anchoring the sheet to the channel bottom and then systematically exciting its free end by vortices shed by a cylinder upstream. The forcing frequency is $f_v = 0.14-2.1$ Hz for different depth-averaged water speeds $U_0 = 22 - 88$ mm s⁻¹, so the cylinder Reynolds number varies between $Re_d \equiv \rho U_0 d_0 / \mu = 240 - 3800$.

Our experiments show that the time-averaged reconfiguration of a thin sheet follows qualitatively the same scaling with the Cauchy number $C_y = 12(C_d \frac{1}{2} \rho U_0^2 / E)(L_b^3 / e_b^3)$ as in the case of a thin sheet in an uniform, steady flow bends, so its time-averaged profile drag is reduced. A simple bending beam model for steady flow which takes into account the drag force, and also the buoyancy force, as in Ref. [50], provides a reasonably good match with observations, if the flow speed U_0 is replaced by that of a local speed based on the depth-averaged steady velocity profile given by Coles law [58]. This suggests that the *average* drag force $\bar{F}_d = C_d 1/2 \rho U_0^2 \bar{h}_b w_b \propto U_0^{2+\mathcal{V}}$. Here, $\bar{h}_b \propto L_b U_0^\mathcal{V}$ is the time-averaged sheet deflection and $\mathcal{V} < 0$ for drag reduction is the so-called Vogel number and is observed to be $\mathcal{V} \approx -0.6 \pm 0.1$ in the present work. The influence of vortices is nonetheless visible for bigger cylinder diameters where there exists a slight lift-up effect leading to a small decrease in the sheet reconfiguration and Vogel exponent. This is attributed to the average velocity defect in the cylinder wake, so the mean sheet *deflection* is given by $\bar{h}_b \sim h_0 - \mathcal{V} l_v$, where h_0 is the deflection in the absence of vortices and l_v is a characteristic length scale of the wake in the vicinity of the sheet tip.

For a given blade thickness (e_b) and length (l_b), the oscillation amplitude (δ_b) of the sheet tip increases with the Reynolds number Re_d . It is also demonstrated that the Cauchy number is the appropriate parameter to scale all data in terms of the nondimensional amplitude δ_b/d_0 . The underlying mechanism that controls sheet-tip oscillations is then analyzed via a toy model which consists of a torsional spring-mounted rigid flat plate subject to an external flow which is decomposed into a uniform steady flow and a regular array of vortices. If the former is taken to control the *average* sheet reconfiguration, the latter is assumed to provide the necessary work for the forced vibration of the sheet. It is then shown that the rescaled oscillation amplitude $\delta_b/d_v \sim C_y^{(1+\mathcal{V})/2} St_v^{-1/2}$, where d_v is the typical length scale of the vortex core and $St_v = f_v d_v / U_0$ the related Strouhal number. So, for a relatively rigid sheet conditions, i.e., for either small or moderate Cauchy numbers in our experiments, $\mathcal{V} \approx 0$, $\delta_b/d_v \sim C_y^{1/2}$. In this case, the sheet vibrates like a rigid curved plate as its local curvature does not change signs over the sheet's entire length. On the other hand, at large Cauchy number $C_y > 10^2$, for a relatively flexible sheet wherein the *average* drag force results in a strong sheet reconfiguration, i.e., when $\mathcal{V} \approx -2/3$ [20], the nondimensional vibration amplitude of the sheet's free end $\delta_b/d_v \sim C_y^{1/6}$. Note that, in the second regime, the sheet exhibits modal oscillations like a flapping flag wherein transverse waves which travel forward towards the sheet's free-end appear (see Supplemental Material [41] for videos).

With respect to the beating frequency (f_b) of the sheet's free end, three dynamical regimes are observed in this study: (i) tip oscillations follow the forcing frequency f_v corresponding to vortex shedding from the upstream cylinder, (ii) tip oscillation frequency is related to vortex shedding behind a free inclined rigid plate of frontal height equal to the *average* sheet deflection \bar{h}_b such that $f_b \sim 0.145 U_h / \bar{h}_b$, and (iii) sheet vibrations occur at one of its natural frequency f_n , near the forcing frequency. When the cylinder diameter $d_0 = 40$ mm, the sheet tip oscillates at the forcing frequency f_v , irrespective of the Cauchy number studied here ($C_y < 10^5$). For smaller cylinders, the sheet displays *flow-induced vibration* controlled by its wake characteristics as in (ii) or a *lock-in*

motion at its natural frequency as in (iii). Furthermore, this transition is possibly dependent on the *average* sheet reconfiguration and sheet thickness as well.

In a classical textbook by Blevins [11], many investigations on flow-induced vibration were classified into two general categories depending on the incoming flow, namely, a steady or an unsteady flow. Our work is a subcategory of the latter case, wherein we provide a case study for interactions between eddies and a flexible sheet. Indeed, more work is necessary to understand and hence predict the above-mentioned dynamical regimes via flow visualization, PIV measurements of the flow around the sheet, and in its wake. The potential effect of sheet confinement is also left for future investigations.

ACKNOWLEDGMENTS

The authors thank S. Martinez from Université Claude-Bernard Lyon1 for his technical support building and maintaining the experimental setup. PIV measurements are collected from an internship work by C. Lehmann. We also acknowledge E. Mäusel and C. Pierrot-Minot for helping us measure some of the sheet's physical and mechanical properties. J.S.J. thanks K. Bruyère for her kind support and guidance with the linear-displacement facility (INSTRON 8802) at Ifstar-TS2, LBMC (Lyon-Bron) to estimate the tensile strength of materials used in this work. This work has benefited from a joint French-German funding support, namely, the DFG-ANR project *ESCaFlex* (ANR-16-CE92-0020, DFG Grant No. 634058).

-
- [1] A. Roshko, On the drag and shedding frequency of two-dimensional bluff bodies, Technical Report No. TN-3169, NACA, 1954.
 - [2] A. Roshko, Experiments on the flow past a circular cylinder at very high Reynolds number, *J. Fluid Mech.* **10**, 345 (1961).
 - [3] E. Berger and R. Wille, Periodic flow phenomena, *Annu. Rev. Fluid Mech.* **4**, 313 (1972).
 - [4] C. H. K. Williamson, Vortex dynamics in the cylinder wake, *Annu. Rev. Fluid Mech.* **28**, 477 (1996).
 - [5] T. Sarpkaya, Vortex-induced oscillations—a selective review, *ASME J. Appl. Mech.* **46**, 241 (1979).
 - [6] P. W. Bearman, Vortex shedding from oscillating bluff bodies, *Annu. Rev. Fluid Mech.* **16**, 195 (1984).
 - [7] T. Sarpkaya, Hydrodynamic damping, flow-induced oscillations, and biharmonic response, *ASME J. Offshore Mech. Arct. Eng.* **117**, 232 (1995).
 - [8] T. Sarpkaya, A critical review of the intrinsic nature of vortex-induced vibrations, *J. Fluids Struct.* **19**, 389 (2004).
 - [9] C. H. K. Williamson and R. Govardhan, Vortex-induced vibrations, *Annu. Rev. Fluid Mech.* **36**, 413 (2004).
 - [10] P. W. Bearman, Circular cylinder wakes and vortex-induced vibrations, *J. Fluids Struct.* **27**, 648 (2011).
 - [11] R. D. Blevins, *Flow-Induced Vibration* (Van Nostrand Reinhold Co., New York, 1977).
 - [12] M. P. Paidoussis, *Fluid-Structure Interactions: Slender Structures and Axial Flow* (Academic Press, London, 1998), Vol. 1.
 - [13] B. M. Sumer and J. Fredsøe, *Hydrodynamics Around Cylindrical Structures*, revised ed. (World Scientific, Singapore, 2006), Vol. 26.
 - [14] E. Naudascher and D. Rockwell, *Flow-Induced Vibrations: An Engineering Guide* (CRC Press, Boca Raton, 2012).
 - [15] M. A. R. Koehl, How do benthic organisms withstand moving water? *Am. Zool.* **24**, 57 (1984).
 - [16] S. Vogel, Drag and flexibility in sessile organisms, *Am. Zool.* **24**, 37 (1984).
 - [17] S. Vogel, Drag and reconfiguration of broad leaves in high winds, *J. Exp. Bot.* **40**, 941 (1989).
 - [18] M. A. R. Koehl, When does morphology matter? *Annu. Rev. Ecol. Evol. Syst.* **27**, 501 (1996).
 - [19] S. Vogel, *Life in Moving Fluids: The Physical Biology of Flow* (Princeton University Press, Princeton, New Jersey, 1994).

- [20] E. de Langre, Effects of wind on plants, *Annu. Rev. Fluid Mech.* **40**, 141 (2008).
- [21] F. P. Gosselin, Mechanics of a plant in fluid flow, *J. Exp. Bot.* **70**, 3533 (2019).
- [22] T. Leclercq and E. de Langre, Reconfiguration of elastic blades in oscillatory flow, *J. Fluid Mech.* **838**, 606 (2018).
- [23] M. J. Shelley and J. Zhang, Flapping and bending bodies interacting with fluid flows, *Annu. Rev. Fluid Mech.* **43**, 449 (2011).
- [24] F. Siniscalchi and V. Nikora, Dynamic reconfiguration of aquatic plants and its interrelations with upstream turbulence and drag forces, *J. Hydraul. Res.* **51**, 46 (2013).
- [25] Y. Jin, J. Kim, and L. P. Chamorro, Instability-driven frequency decoupling between structure dynamics and wake fluctuations, *Phys. Rev. Fluids* **3**, 044701 (2018).
- [26] Y. Jin, J.-T. Kim, L. Hong, and L. P. Chamorro, Flow-induced oscillations of low-aspect-ratio flexible plates with various tip geometries, *Phys. Fluids* **30**, 097102 (2018).
- [27] Y. Jin, J.-T. Kim, Z. Mao, and L. P. Chamorro, On the couple dynamics of wall-mounted flexible plates in tandem, *J. Fluid Mech.* **852**, R2 (2018).
- [28] Y. Jin, J. Kim, S. Fu, and L. P. Chamorro, Flow-induced motions of flexible plates: Fluttering, twisting and orbital modes, *J. Fluid Mech.* **864**, 273 (2019).
- [29] H. M. Nepf, Flow and transport in regions with aquatic vegetation, *Annu. Rev. Fluid Mech.* **44**, 123 (2012).
- [30] J. J. Finnigan, Turbulence in waving wheat. I. Mean statistics and honami, *Boundary Layer Meteorol.* **16**, 181 (1979).
- [31] C. Py, E. de Langre, and B. Mouli a, A frequency lock-in mechanism in the interaction between wind and crop canopies, *J. Fluid Mech.* **568**, 425 (2006).
- [32] F. P. Gosselin and E. de Langre, Destabilising effects of plant flexibility in air and aquatic vegetation canopy flows, *Eur. J. Mech. B Fluids* **28**, 271 (2009).
- [33] J. D. Ackerman and A. Okubo, Reduced mixing in a marine macrophyte canopy, *Funct. Ecol.* **7**, 305 (1993).
- [34] M. Ghisalberti and H. M. Nepf, Mixing layers and coherent structures in vegetated aquatic flows, *J. Geophys. Res.* **107**, 3011 (2002).
- [35] R. Singh, M. M. Bandi, A. Mahadevan, and S. Mandre, Linear stability analysis for *monami* in a submerged seagrass bed, *J. Fluid Mech.* **786**, R1 (2016).
- [36] S. Tschisgale, B. L ohrer, R. Meller, and J. Fr ohlich, Large eddy simulation of the fluid–structure interaction in an abstracted aquatic canopy consisting of flexible blades, *J. Fluid Mech.* **916**, A43 (2021).
- [37] V. Nikora, S. Cameron, I. Albayrak, O. Miler, N. Nikora, F. Siniscalchi, M. Stewart, M. O’Hare, W. Rodi, and M. Uhlmann, Flow-biota interactions in aquatic systems: Scales, mechanisms, and challenges, in *Environmental Fluid Mechanics: Memorial Volume in Honour of Prof. Gerhard H. Jirka*, IAHR Monographs, edited by W. Rodi and M. Uhlmann (CRC Press, Boca Raton, 2012), Chap. 11, p. 217.
- [38] Y. Jin, S. Ji, and L. P. Chamorro, Spectral energy cascade of body rotations and oscillations under turbulence, *Phys. Rev. E* **94**, 063105 (2016).
- [39] S. Barsu, Effets collectifs dans une canop ee mod ele immerg ee, Ph.D. thesis, Universit e Claude Bernard Lyon 1, 2016.
- [40] S. Szepessy and P. W. Bearman, Aspect ratio and end plate effects on vortex shedding from a circular cylinder, *J. Fluid Mech.* **234**, 191 (1992).
- [41] See Supplemental Material at <http://link.aps.org/supplemental/10.1103/PhysRevFluids.8.093801> for videos and more information on vortex shedding characteristics.
- [42] F. Angrilli, S. Bergamaschi, and V. Cossalter, Investigation of wall induced modifications to vortex shedding from a circular cylinder, *J. Fluids Eng.* **104**, 518 (1982).
- [43] S. J. Price, D. Sumner, J. G. Smith, K. Leong, and M. P. Paidoussis, Flow visualization around a circular cylinder near to a plane wall, *J. Fluids Struct.* **16**, 175 (2002).
- [44] S. Sarkar and S. Sarkar, Vortex dynamics of a cylinder wake in proximity to a wall, *J. Fluids Struct.* **26**, 19 (2010).
- [45] S. Barsu, D. Doppler, J. J. S. Jerome, N. Riviere, and M. Lance, Drag measurements in lat-

- erally confined 2D canopies: Reconfiguration and sheltering effect, *Phys. Fluids* **28**, 107101 (2016).
- [46] R. D. Blevins, *Formulas for Dynamics, Acoustics and Vibration* (John Wiley & Sons, Chichester, West Sussex, UK, 2015).
- [47] J. Schindelin, I. Arganda-Carreras, E. Frise, V. Kaynig, M. Longair, T. Pietzsch, S. Preibisch, C. Rueden, S. Saalfeld, B. Schmid *et al.*, Fiji: An open-source platform for biological-image analysis, *Nat. Methods* **9**, 676 (2012).
- [48] J. N. Kapur, P. K. Sahoo, and A. K. C. Wong, A new method for gray-level picture thresholding using the entropy of the histogram, *Comput. vision graph. image process.* **29**, 273 (1985).
- [49] W.-H. Tsai, Moment-preserving thresholding: A new approach, *Comput. vision graph. image process.* **29**, 377 (1985).
- [50] M. Luhar and H. M. Nepf, Flow-induced reconfiguration of buoyant and flexible aquatic vegetation, *Limnol. Oceanogr.* **56**, 2003 (2011).
- [51] S. Alben, M. Shelley, and J. Zhang, Drag reduction through self-similar bending of a flexible body, *Nature (London)* **420**, 479 (2002).
- [52] T. Leclercq and E. de Langre, Drag reduction by elastic reconfiguration of non-uniform beams in non-uniform flows, *J. Fluids Struct.* **60**, 114 (2016).
- [53] M. Luhar and H. M. Nepf, Wave-induced dynamics of flexible blades, *J. Fluids Struct.* **61**, 20 (2016).
- [54] J. Lei and H. M. Nepf, Wave damping by flexible vegetation: Connecting individual blade dynamics to the meadow scale, *Coastal Eng.* **147**, 138 (2019).
- [55] J. Lei and H. M. Nepf, Blade dynamics in combined waves and current, *J. Fluids Struct.* **87**, 137 (2019).
- [56] R. J. Adrian and J. Westerweel, *Particle Image Velocimetry* (Cambridge University Press, New York, 2011).
- [57] F. Gosselin, E. De Langre, and B. A. Machado-Almeida, Drag reduction of flexible plates by reconfiguration, *J. Fluid Mech.* **650**, 319 (2010).
- [58] D. Coles, The law of the wake in the turbulent boundary layer, *J. Fluid Mech.* **1**, 191 (1956).